

# CCP-WSI Blind Test Series 3: CFD-Based Numerical Wave Tank Experiments Employing an Impulse Source Wave Maker

Christian Windt and John V. Ringwood  
Centre for Ocean Energy Research, Maynooth University  
Maynooth, County Kildare, Ireland

Josh Davidson  
Department of Fluid Mechanics, Faculty of Mechanical Engineering  
Budapest University of Technology and Economics, Budapest, Hungary

Pál Schmitt  
Marine Research Group, Queen's University Belfast  
Belfast, Northern Ireland

During the development and optimisation of wave energy converters, numerical wave tanks are useful tools, providing detailed insight into the hydrodynamic performance of devices. Specifically, computational fluid dynamics (CFD)-based numerical wave tanks (CNWTs) can deliver high-fidelity, high-resolution results for a wide range of test conditions. However, CNWTs come at significant computational cost and require more man-hours during model setup, compared to lower-fidelity, frequency domain-based models. The computational costs can only be significantly decreased by improving the numerical solvers or by increasing expenditure on computational power. The required man-hours for the model setup, however, can be reduced by streamlining the setup of CNWTs. To this end, the formulation of best-practice guidelines can expedite this streamlining. A step toward such best-practice guidelines is blind tests. This paper presents the CNWT used for the authors' contribution to the Collaborative Computational Project in Wave-Structure Interaction (CCP-WSI) Blind Test Series 3. In the employed numerical wave tanks, a self-calibrating impulse source wave maker is implemented for wave generation. In addition to the numerical results, and the comparison with the recently disclosed experimental data, the paper presents the spatial and temporal convergence studies, as well as results for the numerical wave maker calibration. The numerical results show average deviations with the experimental data of less than 10%. Furthermore, a correlation between the accuracy of the numerical replication of the wave and the agreement between numerical and experimental device motion is highlighted.

## INTRODUCTION

In recent years, growing concerns of human-induced global warming have fueled the R&D of novel technologies to harness renewable energy resources. Among these resources, marine renewable energies (MREs), and specifically ocean wave energy, show significant potential to contribute to the global energy supply (Falcão, 2010). The harsh ocean environment, in which wave energy converters (WECs) are deployed, poses challenges to the R&D of these devices. Although the energy resource is free, to be commercially viable, the price of the produced energy from a WEC, stemming from capital, operational, and maintenance costs, must be minimised.

To drive down the cost of the produced energy, optimisation of the WEC devices is required, for which numerical wave tanks (NWTs) are a valuable tool. Depending on the implemented equations for the solution of the wave-structure interaction (WSI) problem, different levels of fidelity, at different levels of computational cost, can be achieved (Penalba et al., 2017). Lower-fidelity models, implementing methods based on the Laplace equation

and, thus, assuming inviscid and irrotational fluids, are associated with minimal computational cost and are valuable tools for parametric studies or optimisation algorithms. However, due to the required linearisation of the hydrodynamic equations, lower-fidelity models are only valid when considering linear conditions, i.e., small amplitude waves and device motions. Still assuming irrotational and inviscid fluid, non-linear free-surface deformations can be captured in fully non-linear potential flow solvers, such as OceanWave3D (Engsig-Karup et al., 2009). Furthermore, linear models can be extended to capture non-linear effects, such as viscous drag (Morison et al., 1950) or non-linear Froude-Krylov forces (Babarit et al., 2010).

Higher-fidelity NWTs, such as CFD-based numerical wave tanks (CNWTs), are inherently able to capture all relevant hydrodynamic non-linearities (viscous and rotational fluids, turbulent effects, non-linear free-surface deformation, etc.), by numerically solving the Reynolds-averaged Navier-Stokes (RANS) equations. Thus, CNWTs are valid over a wide range of test conditions and are particularly valuable when modelling WECs under controlled conditions (Davidson et al., 2019), where an energy-maximising controller drives the WEC into resonance with the incident wave, resulting in enhanced device motion, beyond the limit of linear hydrodynamic model validity.

Although high-fidelity hydrodynamic models, such as CNWTs, are essential when modelling non-linear WSI for which linear hydrodynamic models are relatively inaccurate, CNWT models are not yet widely used in the MRE field, due to relatively long

---

Received August 21, 2019; updated and further revised manuscript received by the editors October 17, 2019. The original version (prior to the final updated and revised manuscript) was presented at the Twentieth International Ocean and Polar Engineering Conference (ISOPE-2019), Honolulu, Hawaii, June 16–21, 2019.

KEY WORDS: Wave energy, CCP-WSI Blind Test, impulse wave maker, CFD, numerical wave tank, OpenFOAM, RANS.

run times, the need for specialised CFD expertise and substantial man-hours for the model setup, as well as a lack of confidence in some aspects of CNWT models. The latter can stem from uncertainty in the appropriate use of turbulence models, or time-consuming validation studies against possibly inapt experimental data sets. While the run times will always be significantly longer than those for lower-fidelity models, the setup of CNWT models can be improved by defining guidelines and standards for CNWTs in MRE applications.

One step towards such guidelines and standards is administering blind tests for model validation. High-quality experiments in physical wave tanks (PWTs) are performed, and relevant measurements (e.g., free-surface elevation (FSE) and device motion) are recorded. Participants of the blind tests are given information on the physical setup (tank dimensions, measurement location, body mass, etc.) to replicate the experiment with their CNWT. The results of the CNWT simulations (e.g., FSE and device motion) are then submitted for a blind comparison to the reference results from the PWT experiments. This procedure prevents tuning of numerical models to fit pre-known PWT test results, thereby undermining the confidence and generalisation ability of the CNWT. Recently, a series of blind tests has been conducted as part of the Collaborative Computational Project in Wave–Structure Interaction (CCP-WSI) (Ransley et al., 2019, 2020).

In this paper, the numerical model for the authors' contribution to the CCP-WSI Blind Test Series 3 is presented, and the simulation results are compared to the recently released PWT data. The test series considers a moving, WEC-like structure exposed to focused waves. The CNWT is implemented in the open-source CFD software OpenFOAM (Weller et al., 1998). Waves are generated using a recently developed, self-calibrating, impulse source wave maker (Schmitt et al., 2019). In addition to the numerical results and the comparison to the recently disclosed experimental data, the paper presents the spatial and temporal convergence studies, as well as results for the numerical wave maker calibration. The comparative analysis of the simulation results, submitted by all Blind Test participants, can be found in Ransley et al. (2020).

## Outline of Paper

The remainder of this paper is organised as follows: The setup of the PWT tests is described briefly in the section PWT Tests. Next, in the CNWT Setup section, the setup of the CNWT is presented. The governing equations, as well as details on the implemented wave generation and absorption method, are given. Furthermore, convergence studies of the problem discretisation (spatially and temporally) are presented, and the necessity of turbulence modelling is discussed. Results of the CNWT simulations, together with the PWT data, are presented and discussed in Results and Discussion. Finally, conclusions are drawn.

## PWT TESTS

For the CCP-WSI Blind Test Series 3, PWT experiments were conducted in the the ocean basin of the COAST laboratory at Plymouth University, specifically for the purpose of CNWT validation. The ocean basin is 32.1 m long, 15.65 m wide, 3 m deep, and is equipped with a flap-type wave maker and an absorbing beach. The test campaign includes WSI, as well as wave-only experiments. The results of the wave-only experiments are provided to the blind test participants beforehand, to be replicated as input for the WSI experiments, whereas the PWT results for the WSI are withheld from the participants until after submission of the numerical results. For further details see Ransley et al. (2020).

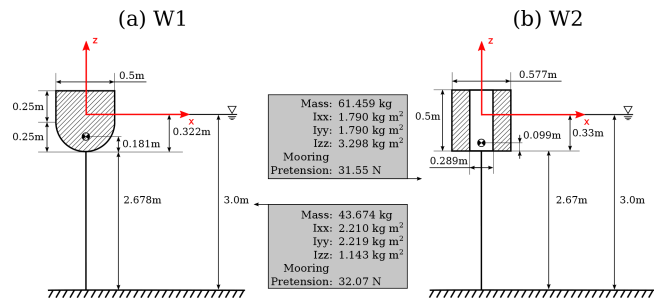


Fig. 1 Schematic of the considered WEC structures

## WEC Structures

Two different WEC structures are considered, W1 and W2, resembling moored point absorber-type devices. Both structures have axisymmetric, cylindrical geometries. All relevant dimensions are shown in Fig. 1. The mooring of the structures is implemented with a linear spring with a stiffness of  $67 \text{ N m}^{-1}$ , connecting the device with the tank floor.

## Input Waves

The test series considers three different focused waves of varying steepness, 1BT3–3BT3, whose characteristics are listed in Table 1. The experimentally measured FSE for each wave at the focus location is plotted in Fig. 2. Note that the FSE is plotted over the relative time  $t_r$ , and all peaks are artificially aligned at  $t_r = 1$  purely for display purposes.

## CNWT SETUP

The CNWT in this study is based on the open-source CFD software OpenFOAM, specifically OpenFOAM version 4.1. The hydrodynamics in the CNWT are captured by solving the incompressible RANS equations, describing the conservation of mass and momentum,

$$\nabla \cdot \mathbf{U} = 0 \quad (1)$$

$$\frac{\partial \rho \mathbf{U}}{\partial t} + \nabla \cdot \rho \mathbf{U} \mathbf{U} = -\nabla p + \nu \nabla \cdot \nabla \mathbf{U} + \rho \mathbf{f}_b \quad (2)$$

respectively. Here,  $t$  denotes time,  $\mathbf{U}$  is the fluid velocity,  $p$  is the fluid pressure,  $\rho$  is the fluid density,  $\nu$  is the kinematic viscos-

	$A_n$ [m]	$f_p$ [Hz]	$d$ [m]	$H_s$ [m]	$\lambda$ [m]	$kA$ [-]
Wave 1BT3	0.2	0.4	3.0	0.274	9.41	0.129
Wave 2BT3	0.3	0.4	3.0	0.274	9.41	0.193
Wave 3BT3	0.32	0.4	3.0	0.274	9.41	0.206

Table 1 Wave characteristics of the considered focused waves

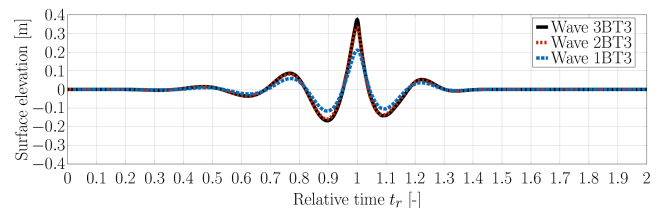


Fig. 2 Experimentally measured FSE of waves 1BT3–3BT3 at the focal location. The time traces are artificially aligned to match the peaks at  $t_r = 1$ .

ity, and  $\mathbf{f}_b$  denotes external forces such as gravity. In the literature, RANS models are the current industry standard (compared to large-eddy simulation models, for example) for the modelling of WECs in CNWTs (Windt et al., 2018), avoiding high computational cost. The water wave advection is captured via the volume-of-fluid method, proposed by Hirt and Nichols (1981), following

$$\frac{\partial \alpha}{\partial t} + \nabla \cdot (\mathbf{U}\alpha) + \nabla \cdot [\mathbf{U}_r \alpha (1 - \alpha)] = 0 \quad (3)$$

$$\Phi = \alpha \Phi_{\text{water}} + (1 - \alpha) \Phi_{\text{air}} \quad (4)$$

where  $\alpha$  denotes the volume fraction of water,  $\mathbf{U}_r$  is the compression velocity (Berberović et al., 2009), and  $\Phi$  is a specific fluid quantity.

The body motion, induced by the incident wave, is solved via Newton's second law of motion within the sixDoFRigidBodyMotionSolver, implemented in the OpenFOAM framework. The motion solver provides a set of motion restraints, allowing the implementation of a linear spring to account for the mooring of the device. The resulting body motion is accommodated in the numerical domain through mesh morphing, delivering computationally efficient and accurate results (Windt, Davidson, Chandar, and Ringwood, 2019).

To measure the FSE, the iso-surface of the volume fraction  $\alpha = 0.5$  is recorded throughout the course of the simulation. The FSE at specific locations, following the layout of the PWT, can be extracted from the iso-surface data in a post-processing step.

### Numerical Wave Generation and Absorption

Different numerical wave makers are available to generate and absorb waves in a CNWT (Miquel et al., 2018). Herein, the impulse source method, proposed by Schmitt et al. (2019), is employed. A source term,  $\mathbf{r}\rho\mathbf{a}_{wm}$ , is added to the RANS momentum equation (2), yielding

$$\frac{\partial \rho \mathbf{U}}{\partial t} + \nabla \cdot \rho \mathbf{U} \mathbf{U} = -\nabla p + \nu \nabla \cdot \nabla \mathbf{U} + \rho \mathbf{f}_b + \mathbf{r}\rho\mathbf{a}_{wm} \quad (5)$$

The location of the wave maker zone is defined by  $\mathbf{r} = 1$ , with  $\mathbf{r} = 0$  everywhere else in the domain.  $\mathbf{a}_{wm}$  is the field variable acting as acceleration input to the wave maker, which can be determined analytically (Choi and Yoon, 2009) or, as applied here, via an iterative calibration method (Schmitt et al., 2019).

To calibrate  $\mathbf{a}_{wm}$ , a standard spectral analysis method based on Masterton and Swan (2008) is adapted to produce a target wave at a specific position within the CNWT, comprising the following steps:

1. Define a target wave time series,  $\eta_T$
2. Perform a fast Fourier transform (FFT) on  $\eta_T$ , to obtain the amplitudes and phases, for each frequency component
3. Define an initial time series for  $\mathbf{a}_{wm,1}$ , serving as input to the OpenFOAM simulation
4. Perform an FFT on  $\mathbf{a}_{wm,1}$ , to obtain the amplitudes and phases for each frequency component of  $\mathbf{a}_{wm,1}$
5. Run the OpenFOAM simulation for calibration iteration  $i$ , using  $\mathbf{a}_{wm,i}$ , and monitor the resulting FSE,  $\eta_{R,i}$ , at the specific CNWT location. Note that, for long crested waves, with an invariant wave field in the lateral direction, simulations can be performed in 2-D domains, to reduce the computational burden.
6. Perform an FFT on  $\eta_{R,i}$ , to obtain the amplitudes and phases for each frequency component of  $\eta_{R,i}$
7. Correct the amplitude components of  $\mathbf{a}_{wm,i}$ , by scaling with the ratio of the  $\eta_T$  and  $\eta_{R,i}$  amplitudes
8. Correct the phase components of  $\mathbf{a}_{wm,i}$ , by summing the phase with the difference between the phase components of  $\eta_T$  and  $\eta_{R,i}$

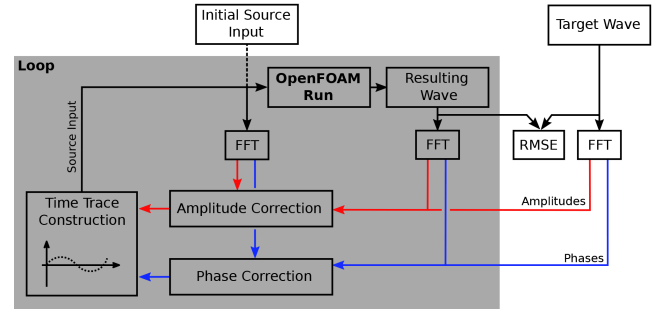


Fig. 3 Calibration scheme for the impulse source input; figure adapted from Schmitt et al. (2019)

9. Construct  $\mathbf{a}_{wm,i+1}$ , using the inverse Fourier transform on the corrected amplitude and phase components

10. Steps 5–9 are repeated either for a maximum number of iterations or until a threshold for the root mean-squared error (RMSE) between the  $\eta_T$  and  $\eta_{R,i}$  is reached.

A schematic of the calibration procedure is depicted in Fig. 3. For further details, the interested reader is referred to Schmitt et al. (2019).

For wave absorption, a numerical beach, proposed by Schmitt and Elsässer (2015), is implemented. Introducing the additional dissipation term,  $\mathbf{S}\rho\mathbf{U}$ , to the RANS momentum equation (Eq. 2), yields

$$\frac{\partial \rho \mathbf{U}}{\partial t} + \nabla \cdot \rho \mathbf{U} \mathbf{U} = -\nabla p + \nu \nabla \cdot \nabla \mathbf{U} + \rho \mathbf{f}_b + \mathbf{S}\rho\mathbf{U} \quad (6)$$

The variable field  $\mathbf{S}$  controls the strength of the dissipation, with a value of zero in the simulation zone, and then gradually increases toward the boundary, over a defined length, following an analytical expression.

To control the absorption quality of the numerical beach, the length and the maximum damping factor,  $\mathbf{S}_{\max}$ , can be adjusted. Based on the findings in Windt, Davidson, Schmitt, and Ringwood (2019), the length of the numerical beach is set to  $1\lambda_{1BT3}$ , while the maximum damping factor varies for the different focused waves. For 1BT3,  $\mathbf{S}_{\max} = 5 \text{ s}^{-1}$  delivers a reflection coefficient,  $R$  (Mansard and Funke, 1980), of  $\leq 1\%$ . For 2BT3 and 3BT3,  $\mathbf{S}_{\max}$  is increased to  $7 \text{ s}^{-1}$  to maintain the small reflection coefficient. A screenshot of the CNWT, showing the field variable  $\mathbf{S}$ , is depicted in Fig. 4a. Screenshots of the field variable  $\alpha$  and  $\mathbf{r}$  are shown in Fig. 4b.

Note that the symmetry of the problem is exploited, and only half of the PWT is modelled numerically. A symmetry boundary

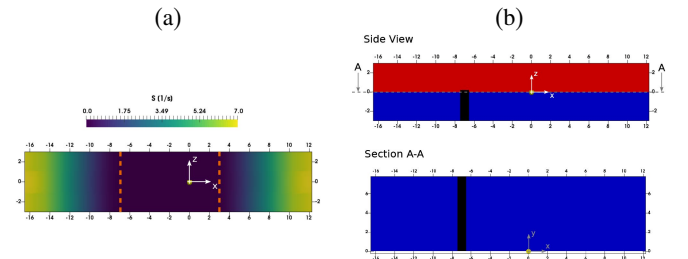


Fig. 4 (a) 2-D screen shots of the CNWT showing the gradually increasing damping factor  $\mathbf{S}$  of the numerical beach. The dashed orange lines indicate the start coordinate of the numerical beaches. (b) The water and air phases (blue and red colour code, respectively), the impulse source (black colour code), and the WEC structure (yellow colour code), which is located at  $(x, y, z) = (0, 0, 0)$

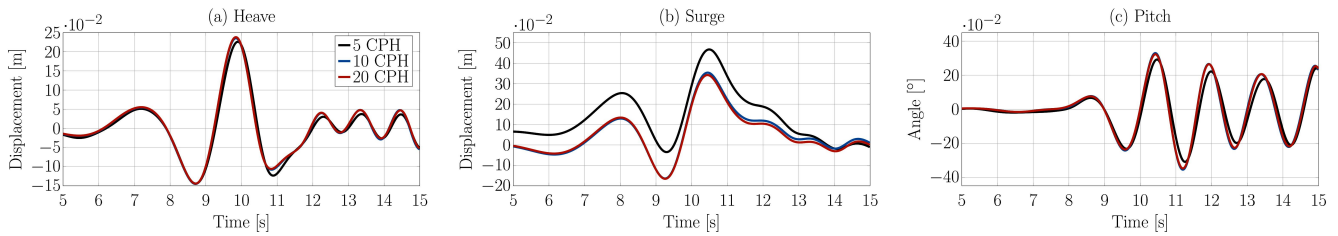


Fig. 5 Motion time traces of W1 for three different cell sizes:  $\Delta z = 0.013, 0.026, 0.052$  m

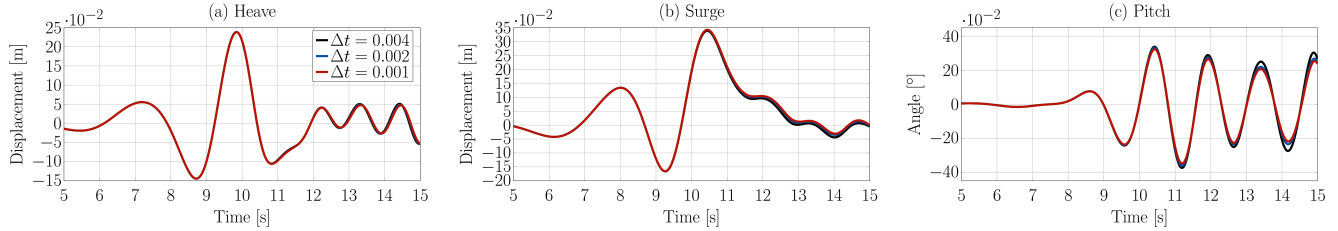


Fig. 6 Motion time traces of W1 for three different time steps:  $\Delta t = 0.001, 0.002, 0.004$  s

condition is employed in the  $x,z$ -plane, where  $x$  points in the wave propagation direction, and  $z$  toward the tank floor. This symmetry condition introduces constraints on the body motion, only allowing motion in three degrees of freedom (DoFs), i.e., heave, surge, and pitch.

**Problem Discretisation**

To determine the spatial and temporal problem discretisation sizes, convergence studies have been performed, preliminary to the final simulations for the blind test. Simulations are run for three different discretisation sizes, i.e., three grid sizes ( $\Delta z = 0.013, 0.026, 0.052$  m) in the free-surface interface zone and around the body, for the spatial convergence study, and three time step sizes ( $\Delta t = 0.001, 0.002, 0.004$  s) for the temporal convergence study.

Note that fixed time step sizes, rather than variable time step sizes with a Courant number,  $Co$ , criterion, have been used for the simulations. The fixed time steps result in a consistently stable performance of the motion solver, while any potential  $Co > 1$  are accounted for by the PIMPLE algorithm (Holzmann, 2016). PIMPLE blends the semi-implicit method for pressure-linked equations (SIMPLE) (Patankar and Spalding, 1972) and the pressure-implicit split-operator (PISO) (Issa, 1986).

The results for the translational (heave and surge) and rotational (pitch) motion are depicted in Figs. 5 and 6, for the spatial and temporal convergence study, respectively. Visual inspection of the time traces in Figs. 5 and 6 shows that converged results are achieved for the motion of the geometry. For the spatial convergence study, all the plotted results show converged results with a grid size of  $\Delta z = 0.026$  m (see the grid layout in Fig. 7), resulting in a total cell count of 1,009,682 for W2 and 962,250 for W1. Similarly, for the temporal problem discretisation, converged results are achieved with a time step size of  $\Delta t = 0.002$  s.

**Turbulence Modelling**

To evaluate if turbulence modelling is required, preliminary simulations, with and without turbulence modelling, are performed. For the turbulence modelling, a standard  $k-\omega$  shear stress transport (SST) turbulence model (Menter, 1992), with standard wall functions for the turbulent quantities, was chosen, based on the review in Windt et al. (2018).

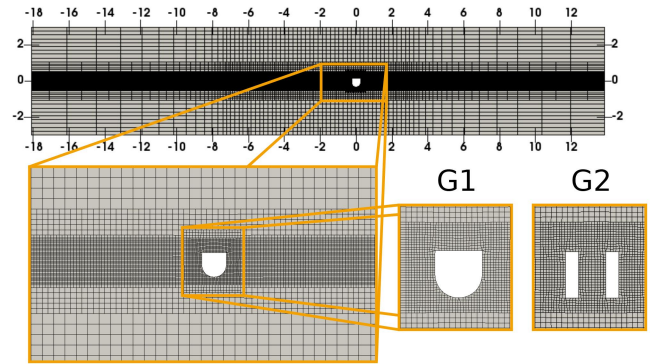


Fig. 7 Spatial discretisation of the CNWT. Mesh grading is employed toward the left and right domain boundaries to reduce the cell count in the numerical beach.

From the preliminary simulations, largest deviations of less than 5% are found for the simulated motion data, with and without turbulence modelling (Windt, Davidson, Schmitt, and Ringwood, 2019). Ultimately, laminar conditions are assumed for the final simulations of the blind test. This is justified by small deviations between laminar and turbulent simulations, the uncertain validity of the applied wall functions (Schmitt and Elsässer, 2017), and the increased run times associated with turbulent simulation.

**RESULTS AND DISCUSSION**

In this section, the numerical results for the different WEC structures and input waves are presented and discussed. Furthermore, a comparison between the PWT and NWT results is shown.

**Wave Maker Calibration**

Before running the WSI simulations, the impulse source wave maker must be calibrated to the desired input waves, plotted in Fig. 2, using the method depicted in Fig. 3. The time traces of the resulting waves 1BT3–3BT3, considered for the final simulations, are plotted in Fig. 8, together with the associated target wave. The numerical waves are chosen based on the minimum RMSE between the target and resulting wave, which, in the presented

cases, coincidences with the minimum deviation at the peak and preceding trough of the focused wave. Given that the agreement between the resulting and target waves at the main peak and preceding trough are specific evaluation criteria for the blind comparison, emphasis is put on these values when calibrating the wave maker.

Qualitatively, a clear trend of the agreement between the target and the resulting wave can be observed, indicating increasing deviations with increasing wave steepness. This trend is confirmed quantitatively by the RMSE. For the waves 1BT3–3BT3, RMSE values of  $0.9 \cdot 10^{-2}$  m,  $1.9 \cdot 10^{-2}$  m, and  $4.2 \cdot 10^{-2}$  m are calculated, respectively. Specifically, after the main peak of the focused wave, relatively large deviations between the target and the resulting wave, in the form of high-frequency components in the resulting wave, can be observed. This problem has been pointed out by Schmitt et al. (2019) and requires future improvement of the calibration method.

### Wave 1BT3

Figures 9(i) and 9(ii) show the comparison of the PWT experiments and CNWT simulations, for the WEC motions and the mooring forces, for W1 and W2, respectively, when exposed to wave 1BT3. Also included in the plots, for insight toward observed differences between the PWT and CNWT results, is the deviation between the generated input wave series in the CNWT and target wave series measured from the PWT.

From a visual inspection, a relatively good, qualitative agreement can be observed between the PWT and CNWT results for the heave and surge motions, as well as the mooring force. Larger deviations are visible in the pitch DoF, particularly after the first peak in the pitch motion time trace, at approximately 10.5 s. Comparing the agreement between the PWT and CNWT pitch motion for W1 and W2, slightly better agreement can be observed for W2. The trend of relatively larger deviations after the peak of the time trace can, indeed, also be observed for the heave and surge motions, as well as the mooring force.

Further inspection of Fig. 9 suggests that the deviation between the numerical and experimental motion and force signals are closely correlated to the disparity between the PWT (target) and CNWT (resulting) surface elevation. This correlation is highlighted in the bar graphs in Fig. 10, via the mean average percentage error (MAPE), following

$$\text{MAPE} = \frac{100\%}{n} \sum_{i=1}^n \left| \frac{y_{\text{exp}}(n) - y_{\text{num}}(n)}{\hat{y}_{\text{exp}}} \right| \quad (7)$$

where  $y_{\text{num}}$  denotes the numerical quantity,  $y_{\text{exp}}$  is the corresponding experimental quantity, and  $\hat{y}_{\text{exp}}$  is the main peak value of the corresponding experimental quantity.  $n$  defines the number of samples and is adjusted based on the considered, temporal signal length via the sampling period. In the following analysis, two different signal lengths,  $W$  and  $P$ , are evaluated for each motion or force signal: ( $W$ ) considering the whole time trace and ( $P$ ) considering the time trace only up until the main peak value of the respective experimental quantity. The motivation for considering the shorter signal is that focused wave experiments are typically performed to calculate extreme loads, which occur at the peak amplitude of the input wave, therefore, a deteriorating simulation accuracy after the peak event is of less importance than ensuring high accuracy leading up to, and during, the peak.

The quantitative results shown in Fig. 10 underpin the qualitative analysis shown in Figs. 9(i) and 9(ii). An error of 1.5% is calculated for the pitch motion of W2 (0.9% for W1), when

only considering the portion of the signals before the experimental peak value. Considering the full signal length, the MAPE for the pitch motion of W2 increases to 11.4% (17.8% for W1), thereby showing the largest deviation of the three DoFs. The pitch motion of the two WECs is mainly affected by the provided inertial properties, the location of the centre of gravity and the centre of rotation. Physically measuring the inertial properties of devices is challenging and prone to measurement uncertainty, which may be the cause of the observed mismatch between the experimental and numerical data.

For the heave and surge motion, as well as the mooring force, MAPE values between 0.9% and 7.3% are calculated, when considering the full signal length. For the shorter signal, the MAPE range decreases to 0.5%–1.5%.

### Wave 2BT3

Figures 9(iii) and 9(iv) show the results for wave 2BT3. Inspecting the absolute deviation between the PWT and CNWT waves, slightly larger deviations can be observed, compared to wave 1BT3, specifically at 6 s within the time trace, at the peak of the focused wave, and the subsequent tail. This larger error in the wave signal is also reflected in the larger deviation between the PWT and CNWT motion and mooring force signals.

The mismatch between the target and resulting wave at 6 s within the time trace is reflected, with some delay (approximately 1 s), in the measured WEC motion data and the mooring forces. The effect of the mismatch before the main wave peak is, however, only short-lived, and relatively good agreement between the experimental and numerical data is achieved between the initial mismatch up until the main target wave peak. The mismatch of the target wave, and the subsequent mismatch between the experimental and numerical WEC motion and mooring force data could potentially be eliminated by considering several wave probes during wave calibration, ensuring better wave propagation.

The pitch motion again shows, qualitatively and quantitatively, the largest error. A visual inspection of the pitch motion time traces reveals a phase shift between the experimental and numerical pitch motion data after the main peak, following the same trend as for wave 1BT3. Quantitatively, MAPE values of approximately 16% for both WEC structures are calculated, when considering the full signal length (see Fig. 10). This MAPE value drops to 2.1% and 3.7% for WEC structures W1 and W2, respectively, when only considering the signal up to the peak, thereby again following the trend observed in the results for wave 1BT3.

For heave and surge motions, as well as the mooring force, MAPE values between 1.9% and 9.9% are calculated, when considering the full signal length. For the shorter signal, the range of MAPE values decreases to 0.8%–4.5%. These increased error values for the full signals correlate with the larger errors between the PWT and CNWT wave signals after the focused wave peak.

### Wave 3BT3

Figures 9(v) and 9(vi) show the results for wave 3BT3. In Figs. 9(v) and 9(vi), a larger deviation between the PWT and CNWT wave signal can be observed, compared to waves 1BT3 and 2BT3. Correspondingly, there is poor agreement between the PWT and CNWT WEC motion and mooring force data. The errors in the CNWT data for almost all the considered quantities, and for both signal lengths, are increased, compared to waves 1BT3 and 2BT3 (see Fig. 10). It is, however, expected that the agreement between the PWT and CNWT WEC motion and mooring force data can be improved, when exposing the WEC to more accurate numerical replication of the desired focused wave.

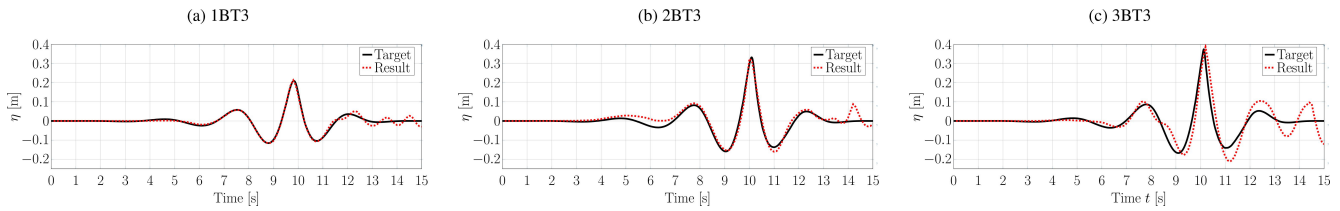


Fig. 8 Target (solid black line) and resulting wave (dashed red line) used in the final WSI simulations

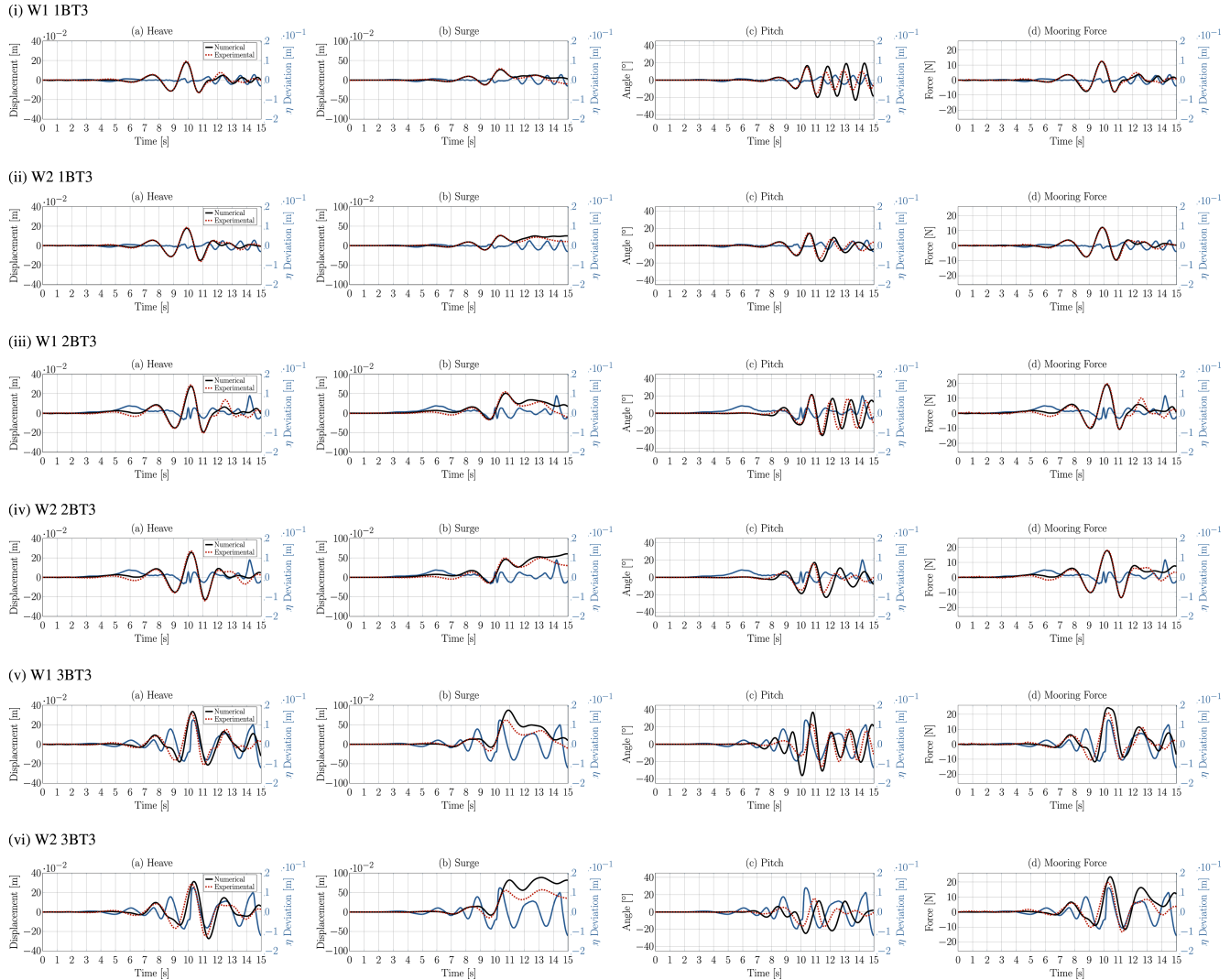


Fig. 9 Motion and force time traces for W2, exposed to wave 3BT3

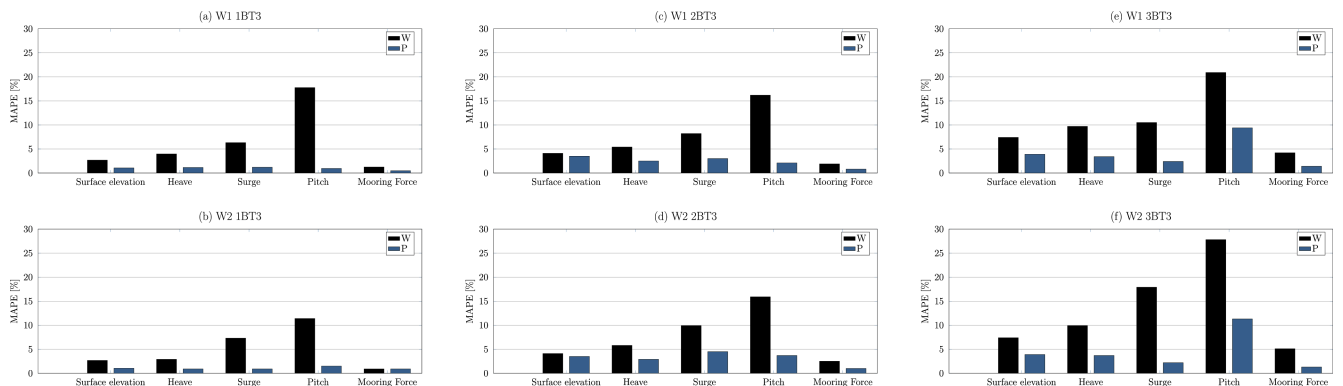


Fig. 10 MAPE [%] between the experimental motion and force data, considering the whole time trace (W), as well as the time trace only up until the peak value of the respective experimental quantity (P)

	Wave 1BT3	Wave 2BT3	Wave 3BT3
Wave-only	710	723	739
W1	2476	2502	2608
W2	2486	2501	2504

Table 2 Relative run time

### Computational Cost

The computational cost for the different test cases, by means of the relative run time  $\bar{t}_{rt} = t_{rt}/t_{st}$ , where  $t_{rt}$  is the absolute run time and  $t_{st}$  is the simulated time (i.e., 15 s), is listed in Table 2. All computations were performed on  $23 \times 2.4$  GHz cores.

### CONCLUSIONS

This paper presents the numerical model and the results for a contribution to the CCP-WSI Blind Test Series 3, including a comparison between the numerical results and the recently released experimental data. An acceptable agreement between the numerical and experimental data is found for the focused waves 1BT3 and 2BT3, but less so for the larger-amplitude wave 3BT3. Specifically, in the time trace before the main peak of each quantity, relatively small errors of less than 5% are observed. Based on the recent literature review presented by Windt et al. (2018), the agreement between the numerical and experimental results falls well within the range of typically achieved accuracy during CNWT validation. Given that focused waves are commonly employed for the analysis of extreme loads, these main peaks are most important, highlighting the value of the presented numerical model in such applications.

The main conclusion to be drawn from the results presented in this paper is that, in order to validate a CNWT by replicating a PWT experiment, it is essential to reproduce the input wave signal with high accuracy. The results shown in this paper demonstrate a strong correlation between the error in the CNWT WEC motion, and mooring force data, with the error in the surface elevation signal. Further guidelines can be derived from a code-to-code comparison, which is presented by Ransley et al. (2020).

### ACKNOWLEDGEMENTS

This paper is based upon work supported by Science Foundation Ireland under Grant No. 13/IA/1886. The research reported in this paper was furthermore supported by the Higher Education Excellence Program of the Ministry of Human Capacities in the framework of the Water Science and Disaster Prevention research area of Budapest University of Technology and Economics (BME FIKP-VÍZ).

### REFERENCES

Babarit, A, Mouslim, H, Clément, A, and Laporte-Weywada, P (2010). "On the Numerical Modelling of the Nonlinear Behaviour of a Wave Energy Converter." *Proc 28th Int Conf Ocean Offshore Arct Eng*, Honolulu, HI, USA, ASME, 4, 1045–1053. <https://doi.org/10.1115/OMAE2009-79909>.

Berberović, E, van Hinsberg, NP, Jakirlić, S, Roisman, IV, and Tropea, C (2009). "Drop Impact onto a Liquid Layer of Finite Thickness: Dynamics of the Cavity Evolution," *Phys Rev E*, 79, 036306-1–036306-15. <https://doi.org/10.1103/PhysRevE.79.036306>.

Choi, J, and Yoon, SB (2009). "Numerical Simulations Using Momentum Source Wave-maker Applied to RANS Equation Model," *Coastal Eng*, 56(10), 1043–1060. <https://doi.org/10.1016/j.coastaleng.2009.06.009>.

Davidson, J, Windt, C, Giorgi, G, Genest, R, and Ringwood, JV (2019). "Evaluation of Energy Maximising Control Systems for Wave Energy Converters Using OpenFOAM," In *OpenFOAM*, Springer, 157–171.

Engsig-Karup, AP, Bingham, HB, and Lindberg, O (2009). "An Efficient Flexible-order Model for 3d Nonlinear Water Waves," *J Comput Phys*, 228(6), 2100–2118. <https://doi.org/10.1016/j.jcp.2008.11.028>.

Falcão, AFDO (2010). "Wave Energy Utilization: A Review of the Technologies," *Renewable and Sustainable Energy Rev*, 14(3), 899–918. <https://doi.org/10.1016/j.rser.2009.11.003>.

Hirt, CW, and Nichols, BD (1981). "Volume of Fluid (VOF) Method for the Dynamics of Free Boundaries," *J Comput Phys*, [https://doi.org/10.1016/0021-9991\(81\)90145-5](https://doi.org/10.1016/0021-9991(81)90145-5).

Holzmann, T (2016). *Mathematics, Numerics, Derivations and Open-FOAM*, Holzmann CFD.

Issa, RI (1986). "Solution of the Implicitly Discretised Fluid Flow Equation by Operator-splitting," *J Comput Phys*, 62, 40–65. [https://doi.org/10.1016/0021-9991\(86\)90099-9](https://doi.org/10.1016/0021-9991(86)90099-9).

Mansard, E, and Funke, E (1980). "The Measurement of Incident and Relected Spectra Using a Least Squares Method," In *Proc Int Conf Coastal Eng*, Sydney, Australia, 154–172.

Masterton, S, and Swan, C (2008). "On the Accurate and Efficient Calibration of a 3D Wave Basin," *Ocean Eng*, 35(8), 763–773. <https://doi.org/10.1016/j.oceaneng.2008.02.002>.

Menter, FR (1992). *Improved Two-equation  $k\omega$  Turbulence Models for Aerodynamic Flows*, Technical report, NASA Technical Memorandum TM-103975.

Miquel, A, Kamath, A, Alagan Chella, M, Archetti, R, and Bihs, H (2018). "Analysis of Different Methods for Wave Generation and Absorption in a CFD-based Numerical Wave Tank," *J Mar Sci Eng*, 6(2), 73. <https://doi.org/10.3390/jmse6020073>.

Morison, J, Johnson, J, and Schaaf, S (1950). "The Force Exerted by Surface Waves on Piles," *J Pet Technol*, 2(05), 149–154. <https://doi.org/10.2118/950149-G>.

Patankar, S, and Spalding, D (1972). "A Calculation Procedure for Heat, Mass and Momentum Transfer in Three-dimensional Parabolic Flows," *Int J Heat Mass Transfer*, 15, 1787–1806. [https://doi.org/10.1016/0017-9310\(72\)90054-3](https://doi.org/10.1016/0017-9310(72)90054-3).

Penalba, M, Giorgi, G, and Ringwood, JV (2017). "Mathematical Modelling of Wave Energy Converters: A Review of Nonlinear Approaches," *Renewable Sustainable Energy Rev*, 78, 1188–1207. <https://doi.org/10.1016/j.rser.2016.11.137>.

Ransley, E, et al. (2019). "A Blind Comparative Study of Focused Wave Interactions with a Fixed FPSO-like Structure (CCP-WSI Blind Test Series 1)," *Int J Offshore Polar Eng*, ISOPE, 29(2), 113–127. <https://doi.org/10.17736/ijope.2019.jc748>.

Ransley, E, et al. (2020). "A Blind Comparative Study of Focused Wave Interactions with Floating Structures (CCP-WSI Blind Test Series 3)," *Int J Offshore Polar Eng*, ISOPE, 30(1), 1–10. <https://doi.org/10.17736/ijope.2020.jc774>.

Schmitt, P, and Elsässer, B (2015). "A Review of Wave Makers for 3D Numerical Simulations," In *MARINE 2015 – Computational Methods in Marine Engineering VI, Rome, Italy*, 437–446.

Schmitt, P, and Elsässer, B (2017). "The Application of Froude Scaling to Model Tests of Oscillating Wave Surge Converters," *Ocean Eng*, 141, 108–115. <https://doi.org/10.1016/j.oceaneng.2017.06.003>.

- Schmitt, P, Windt, C, Davidson, J, Ringwood, J, and Whittaker, T (2019). “The Efficient Application of an Impulse Source Wave Maker to CFD Simulations,” *J Mar Sci Eng*, 7(3), 71. <https://doi.org/10.3390/jmse7030071>.
- Weller, HG, Tabor, G, Jasak, H, and Fureby, C (1998). “A Tensorial Approach to Computational Continuum Mechanics Using Object-oriented Techniques,” *Comput Phys*, 12, 620–631. <https://doi.org/10.1063/1.168744>.
- Windt, C, Davidson, J, Chandar, D, and Ringwood, J (2019). “On the Importance of Advanced Mesh Motion Models in CFD-based Numerical Wave Tanks for WEC Testing,” In *MARINE 2019 – Computational Methods in Marine Engineering VIII, Gothenburg, Sweden*, 145–156.
- Windt, C, Davidson, J, and Ringwood, J (2018). “High-fidelity Numerical Modelling of Ocean Wave Energy Systems: A Review of CFD-based Numerical Wave Tanks,” *Renewable Sustainable Energy Rev*, 93, 610–630. <https://doi.org/10.1016/j.rser.2018.05.020>.
- Windt, C, Davidson, J, Schmitt, P, and Ringwood, JV (2019). “Contribution to the CCP-WSI Blind Test Series 2: CFD-based Numerical Wave Tank Experiments Employing an Impulse Source Wave Maker,” *Proc 13th Eur Wave Tidal Energy Conf*, Naples, Italy, 1265-1–1265-10.